

An Axisymmetric Direct Kinetic Solver for Simulation of Hollow Cathode Plasmas

IEPC-2019-331

*Presented at the 36th International Electric Propulsion Conference
University of Vienna, Austria
September 15-20, 2019*

Alexander R. Vazsonyi*
University of Michigan, Ann Arbor, Michigan, 48109, USA

and

Iain D. Boyd†
University of Colorado, Boulder, Colorado, 80309, USA

Understanding the dynamics of hollow cathode plasmas is essential to predicting operational lifetime and the effects on overall thruster operation. A deterministic, kinetic analysis of neutral and ion particles in a thermionic hollow cathode plasma is conducted using an axisymmetric, or 2D3V, Eulerian solver. Unique schemes accounting for the Coriolis and centrifugal forces are utilized to solve the axisymmetric Boltzmann equation. The neutral solver is verified with the direct-simulation Monte Carlo (DSMC) code, MONACO, while the collision algorithm is validated with a Sod shock tube solution. Axisymmetric simulations of the NSTAR discharge hollow cathode geometry are detailed, utilizing a Boltzmann relation plasma, and ion dynamics in the plume are analyzed. A case with a linearly increasing potential profile in the plume is also analyzed, where significant ion backstreaming is observed. Velocity distribution functions (VDFs) of the ions are discussed along the cathode centerline boundary, while ion energy distribution functions (IEDFs) along the plume wall boundary are assessed. Difficulties in capturing plume properties without the inclusion of ion-acoustic turbulence are discussed, highlighting possible avenues for future work, including the addition of charge exchange collisions and an explicit electron model.

*Ph.D. Candidate, Department of Aerospace Engineering, vazsonyi@umich.edu.

†H.T. Sears Memorial Professor, Department of Aerospace Engineering Sciences, iain.boyd@colorado.edu.

Nomenclature

e	= elementary charge, C
E_z	= axial electric field, V/m
E_r	= radial electric field, V/m
f	= velocity distribution function
f_{eq}	= equilibrium velocity distribution function
F_i	= flux term
k_b	= Boltzmann constant, J/K
m	= particle mass, kg
n_i	= ion number density, $1/m^3$
n_n	= neutral number density, $1/m^3$
n_o	= reference ion number density, $1/m^3$
P_n	= neutral pressure, Pa
Q_i	= ionization source term
r	= radial position, m
R	= specific gas constant, $J/(mol \cdot K)$
t	= time, s
T_e	= electron temperature, eV
T_n	= neutral temperature, K
T_o	= reference temperature, K
T_{ref}	= reference temperature for VHS model, K
v_r	= radial velocity, m/s
v_θ	= azimuthal velocity, m/s
v_z	= axial velocity, m/s
z	= axial position, m
α	= accomodation coefficient
β	= ion loss coefficient
δ	= VHS constant
μ_{ref}	= reference viscosity for VHS model, $Pa \cdot s$
ϕ	= electric potential, V
ϕ_i	= flux limiter
ω	= radial/azimuthal velocity angle, <i>radians</i>
ρ	= mass density, kg/m^3
τ	= relaxation time, s
θ	= azimuthal position, m
ξ	= radial/azimuthal velocity magnitude, m/s
ζ	= empirical ionization rate coefficient

I. Introduction

Thermionic hollow cathodes are devices used for generating a cold, dense plasma. They operate by heating a low work function insert held within a cylindrical cavity, where thermionic emission produces an electron current that subsequently ionizes an inflowing propellant gas. A plasma flow escapes this insert region through an orifice at the end of the tube, which is often of a smaller diameter, whereupon it rapidly expands into the plume. In many cases, an additional component known as the ‘keeper’ is placed outside the orifice to protect the cathode body from backstreaming ion particles.

Hollow cathodes have seen significant use in the electric propulsion community; specifically, they are critical for the operation of ion and Hall thrusters, which represent some of the most mature technologies in the field that are capable of providing reasonably high specific impulse.^{1,2} Increasingly stringent mission

requirements in both thruster power and mission lifetime have put increased emphasis on understanding and mitigating any life-limiting processes that are present in these devices. Significant erosion has been observed in hollow cathode devices when operated for long durations, posing a barrier to the consideration of these thrusters for deep space missions.³⁻⁵ To better understand the operation of these devices, and to avoid costly experimental campaigns, various numerical tools have been developed to study hollow cathodes. These have been successful in capturing bulk properties of the plasma.⁶⁻⁸

There are, however, aspects of hollow cathode operation which prove difficult for both full-fluid and even particle-kinetic codes to capture. For example, the gas flow of the cathode is in the continuum regime in the emitter region, transitional in the orifice, and later rarefied in the plume.⁹ To properly capture the evolution of the gas, particularly in the plume, a generalized approach is necessary which can resolve both viscous and rarefied flows. Additionally, understanding the evolution of ion properties in the plume is of critical concern. The plasma in the plume of the cathode is subject to ion-acoustic turbulence (IAT), which has been identified as a source of ions in excess of the discharge voltage that could play a disproportionately large role in erosion of the keeper.^{10,11} In this instability, ions indirectly gain energy at the expense of electrons through the wave-particle interaction known as Landau damping. Ion temperature has been found to increase with distance from the cathode orifice and shows correlation with the magnitude of IAT wave energy.¹² Recent experimental work has also identified two distinct populations of ions in the plume, one ‘slow’ and one ‘fast,’ with the fast population undergoing significant bulk acceleration.¹³ The cause of this acceleration is currently unknown, yet is important to understand as it relates to erosion of the keeper.

Furthermore, there exist other processes in the cathode plume which are poorly understood. Hollow cathodes are characterized by two distinct modes of operation: the ‘spot’ mode and the ‘plume’ mode. The spot mode is considered to be the nominal operating condition of the cathode, with a stable extracted current and low levels of erosion. On the other hand, the plume mode is a ‘noisy’ condition where erosion levels are much higher, and the extracted current is unsteady.¹⁴ While empirical relations have been developed to understand the operating conditions that lead to onset of the plume mode, the mechanisms which cause this mode transition are unknown. Recent work indicates this mode involves an ionization instability that is driven by varying resistivity due to IAT.^{15,16} Understanding the heavy particle dynamics in the rarefied plume region is critical to understanding how such an ionization instability develops.

The necessity of understanding ion dynamics in hollow cathode plumes motivates the use of a kinetic method for simulation. Additionally, the time-dependent behavior of plasma instabilities found in the plume, coupled with the full spectrum of continuum-to-rarefied flow regimes, emphasize the utility of using a noiseless scheme with limited assumptions about the state of the heavy particles. Thus, this research aims to develop an axisymmetric, deterministic kinetic solver for hollow cathodes in order to provide insight for neutral and ion plume dynamics, allowing a more detailed understanding of the processes which drive increased erosion levels and shortened operational lifetimes. In this paper, the implemented numerical methods will be detailed, followed by verification of these methods and application of the solver to a hollow cathode geometry.

II. Methodology

The solver herein solves the Boltzmann equation over discretized phase space (and thus is often referred to as a direct-kinetic [DK] method); in other words, the velocity distribution function (VDF) is explicitly accounted for via discrete bins in velocity space. This approach has the advantage of being free from numerical noise inherent to stochastic methods, such as direct simulation Monte Carlo¹⁷ (DSMC) and particle-in-cell¹⁸ (PIC). While this approach allows for accurate assessment of gas and plasma flows, it is important to note that the VDF is never precisely captured, as only a finite range of velocity space is able to be considered computationally. A cell-centered finite volume scheme is used in physical and velocity space. Temporal advance is achieved through first-order Explicit Euler, with the ability to extend to second- and fourth-order Runge Kutta (RK) schemes.^{19,20}

The assumption of azimuthal symmetry is often used for hollow cathodes and is also adopted here. This means that any terms with variation in the azimuthal component of physical space, θ , are ignored. However, the same is not true for azimuthal velocity, or v_θ space: in equilibrium, particles occupy the VDF non-uniformly in v_θ space, following a Maxwell-Boltzmann distribution. Therefore, one cannot neglect variation in v_θ , and the domain of interest for this work consists of the dimensions: $(z, r, v_z, v_r, v_\theta)$, which is otherwise described as 2D3V.

A. Ions

When simulating an azimuthally symmetric geometry, a coordinate transformation from Cartesian to cylindrical coordinates is prudent. Accounting for the Lorentz force, but neglecting any magnetic field, yields the axisymmetric Boltzmann equation for unmagnetized ions:

$$\frac{\partial f}{\partial t} + v_z \frac{\partial f}{\partial z} + v_r \frac{\partial f}{\partial r} + \frac{eE_z}{m} \frac{\partial f}{\partial v_z} + \left(\frac{v_\theta^2}{r} + \frac{qE_r}{m} \right) \frac{\partial f}{\partial v_r} - \frac{v_\theta v_r}{r} \frac{\partial f}{\partial v_\theta} = Q_i \quad (1)$$

in which the coordinate transform introduces the centrifugal and Coriolis accelerations, whose magnitudes depend on position in velocity space.²¹ These terms introduce a strict CFL condition, which must be respected when evaluating velocity fluxes; to speed up simulation runtime, substepping is performed to ensure this condition is satisfied for larger time steps. To evaluate the VDF, velocity space is discretized in a linear Cartesian manner (see left side of Figure 1). Physical advection in z -space and velocity advection is completed with a MUSCL scheme using a modified Arora-Roe limiter (see [22] for further details), which provides second-order accuracy. In r -space, advection is completed with a centered three-point scheme using a min-mod limiter, which also affords second-order accuracy. Equation 2 gives the expression for flux from the upper side of a finite volume cell,

$$F_{j+1/2} = \frac{1}{2} \left(v_r (f_{j+1}^n + f_j^n) + |v_r| (\Delta f_{j+1/2}^n - \phi_{j+1/2}) \right) \quad (2)$$

where f represents the VDF value, j is the radial index, n is the temporal index, and ϕ is the flux limiter. Ionization events are the only collisions considered for ions. The ionization term, Q_i , is evaluated based on the expression:

$$Q_i = n_i n_n \zeta(T_e) \quad (3)$$

where the ionization rate coefficient, $\zeta(T_e)$, is taken from [23].

B. Neutrals

The centrifugal and Coriolis accelerations present a unique challenge, as their accurate representation is crucial to maintain an equilibrium distribution. These accelerations act in a circular manner in the (v_r, v_θ) plane, whereby a Cartesian discretization of velocity space introduces significant numerical error into the scheme; this error can cause an equilibrium distribution to disequilibrate with no outside forcing.²¹ In order to remedy this, a change of variables to discretize velocity space in a polar manner is useful, as numerical error is significantly reduced (see right side of Figure 1).²⁴ By defining new velocity variables, (ξ, ω) , and representing the radial and azimuthal velocities as $(v_r, v_\theta) = (\xi \cos \omega, \xi \sin \omega)$, the axisymmetric Boltzmann equation for neutrals becomes:

$$\frac{\partial f}{\partial t} + v_z \frac{\partial f}{\partial z} + \xi \cos(\omega) \frac{\partial f}{\partial r} - \frac{\xi}{r} \frac{\partial \sin(\omega) f}{\partial \omega} = -Q_i + \frac{1}{\tau} (f_{eq} - f) \quad (4)$$

In ω -space, advection is completed with the T-UCE operator from [24]. In addition to ionization events, collisions between neutral particles are accounted for via the ellipsoidal statistical Bhatnagar-Gross-Crook, or ES-BGK, operator. This operator is evaluated via an implicit-explicit (IMEX) scheme in time, avoiding the strict CFL condition that would be imposed by the relaxation time, τ , in dense regimes.²⁵ The relaxation time is found via the Variable Hard Sphere (VHS) model, given in Equation 5.

$$\tau^{-1} = \frac{T_{ref}^\delta}{\mu_{ref}} \rho R T^{1-\delta} \quad (5)$$

C. Electrons and Plasma

The plasma in the cathode is considered quasineutral ($n_e \approx n_i$), and the Boltzmann relation is used to determine plasma potential:

$$\phi = \frac{k_b T_e}{e} \ln \left(\frac{n_i}{n_o} \right) + \phi_o \quad (6)$$

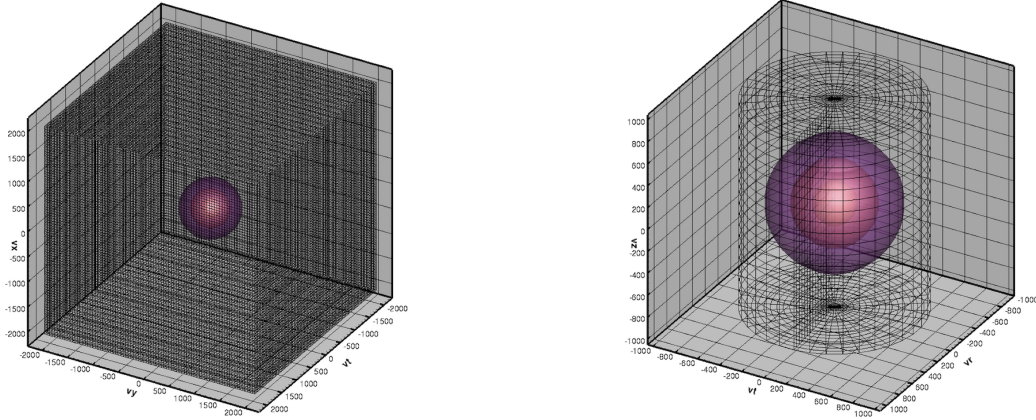


Figure 1: Example VDF iso-surfaces in 3V Cartesian (L) & Cylindrical (R) space.

This model for the plasma approximates the electrons as a massless fluid which perfectly follows the ions; therefore, no properties of the electrons themselves are calculated. The model is used for its ease of implementation and low computational cost, at the expense of a more physical description of the electrons. From this potential, the electric field is obtained from a second-order central finite-difference scheme. The electron temperature is assumed fixed, based on experimental data available for the given cathode.

D. Boundary Conditions

Boundaries are required in all of phase space; for velocity space, the bounds ($v \in [v_{min}, v_{max}]$) are set to be large enough so that the VDF value at the boundary is negligible, and the flux is set to zero to ensure conservation of mass. In physical space, the boundaries are as follows: inflow, outflow, wall, and symmetry. These conditions are elucidated here.

1. Inflow

At the inflow, neutral particles are introduced through setting the value of a ghost cell to a Maxwellian distribution with the desired input conditions. The number density of inflowing neutrals is calculated via Equation 7, where the backpressure is based on the cathode geometry.²³ Xenon is used as the neutral gas in all cases considered here. Backflowing neutrals and ions are allowed to exit the domain.

2. Outflow

At the outflow, neutral and ion particles are allowed to leave the domain. Ghost cells at the outflow may either be set to a vacuum condition or to a Maxwellian at some finite backpressure and temperature. If a backpressure is assigned, the incoming neutral density is calculated using the ideal gas law.

3. Wall

For neutrals, wall collisions are accounted for via an accommodation coefficient, α , and may therefore be diffuse, specular or partially diffuse. Ion wall collisions are accounted for with a loss coefficient, β , and any ions lost to the wall are reintroduced as neutrals.

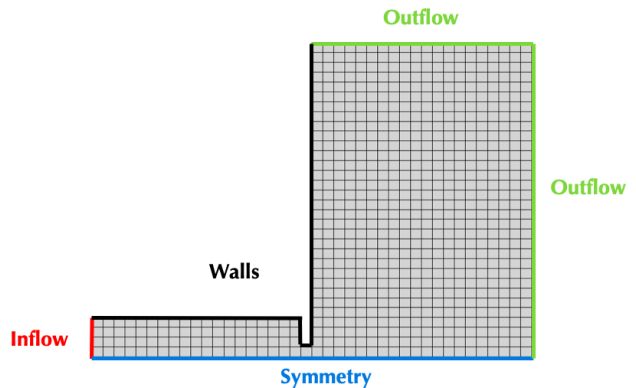


Figure 2: Boundary conditions for a typical cathode geometry.

4. Centerline

The centerline condition tracks any particles leaving the domain and reintroduces them, via ghost cells, to enter the domain by mirroring the VDF value in the velocity space of the boundary-normal direction.

$$n_n = 9.65 \times 10^{24} * \frac{P_n}{T_n} [1/m^3] \quad (7)$$

III. Results & Discussion

A. Collision Operator Verification

The ES-BGK operator with IMEX temporal advance is first tested in a 1D1V Sod shock tube problem, a well-studied problem in gas dynamics.²⁶ In the physical setup, two gas populations are introduced on either side of a diaphragm. At some time, the diaphragm bursts and the gases are allowed to mix. Analogously, in the simulation, two distinct gas populations are initialized on either side of a boundary. At time $t = 0$, the gases are allowed to evolve, which mimics the burst of the physical diaphragm. The initial gases are assumed to be equilibrium, non-drifting populations: left side (L) gas properties are given here with respect to those on the right side (R) of the boundary: $\rho_L = 5.25\rho_R, T_L = 6.75T_R$. $N_x = 2000$ grid points are used in physical space, while $N_v = 120$ grid points are used in velocity space. A timestep of $\Delta t = 1ns$ is used and the simulation is allowed to run for $10 \mu s$. For comparison with the simulation, an exact Riemann problem is solved with identical initial conditions. An arbitrary time in the simulation is chosen for this comparison.

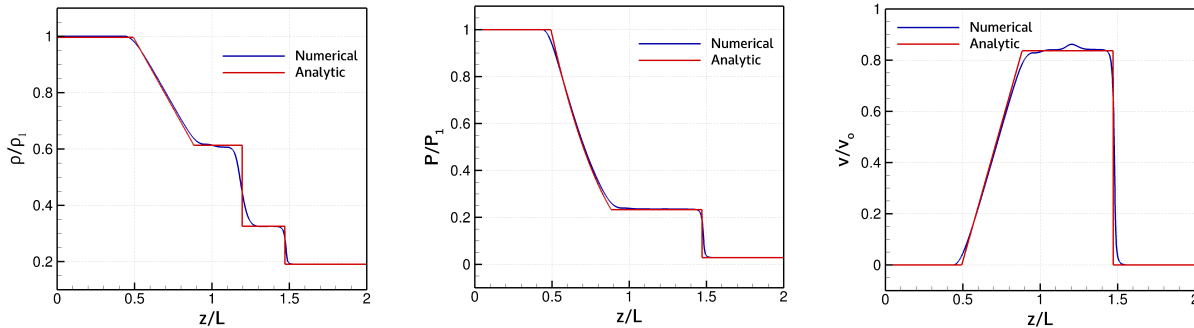


Figure 3: ES-BGK algorithm verification. Density (L), pressure (C), and velocity (R) are shown.

Density and pressure values in Figure 3 are given normalized to the left-side initial conditions, while the velocity is normalized to the thermal velocity at T_L . A shock is present around $z/L = 1.5$, a contact discontinuity is present around $z/L = 1.2$, and a rarefaction fan spans between $z/L = 0.5 - 0.9$. As is evident in the Figure, the numerical results show excellent agreement with the analytic profiles. There exists some numerical dissipation, as is expected for a hyperbolic scheme, near the sharp gradients. In addition, there is a slight oscillation in the velocity at $z/L = 1.2$, at the contact discontinuity, which causes some discrepancy. Nonetheless, these results indicate the collision operator is implemented correctly and may be used in further investigation.

B. Neutral Solver Verification

Before applying the plasma solver to a cathode geometry, a verification test of the neutral flow is conducted, using the DSMC code, MONACO.²⁷ The geometry chosen for this verification is the NSTAR discharge cathode, for which there exists a large amount of experimental and numerical data.²⁸⁻³⁰ The details of the applied simulation conditions are given in Table 1. An assumption of zero azimuthal drift velocity is made, allowing only half the VDF to be simulated in ω ; this reduces memory requirements and simulation wall time. The DSMC simulation utilizes an identical physical domain and boundary conditions, though more physical cells are needed to satisfy the condition of cell size smaller than the local mean-free-path. The DSMC case is run for 50,000 steps, then time-averaged over 100,000 additional steps to ensure smooth results. An adaptive cell weighting technique is used to ensure at least 30 macroparticles are present in each computational cell, for statistical significance.

Δt (s)	$5x10^{-8}$
Total Steps	25,000
Channel Length (cm)	2.0
Channel Width (cm)	0.2
Plume Length (cm)	2.0
Plume Width (cm)	1.6
Orifice Length (cm)	1.0
Orifice Width (cm)	0.5
N_Z	40
N_R	64
T_{wall} (K)	1350

(a) Domain conditions.

V_Z (m/s)	[-1300,1300]
ξ (m/s)	[0,1300]
ω (deg)	[0,180]
N_{V_Z}	26
N_ξ	260
N_ω	18
α	1.0
δ	0.85
Q (SCCM)	3.6
n_{inlet} (m^{-3})	$2.20x10^{22}$
T_{inlet} (K)	1350

(b) Neutral flow conditions.

Table 1: Simulation conditions for the verification case. The domain conditions are given on the left, while the neutral flow conditions are given on the right.

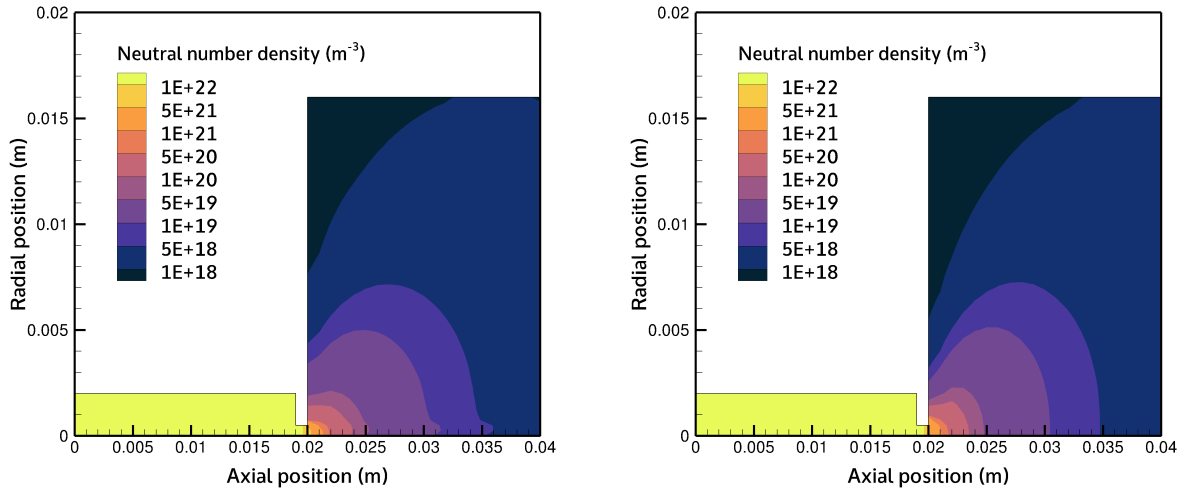


Figure 4: 2D density comparison between the DK code (left) and DSMC (right).

Figure 4 gives the density contours for the DK code and the DSMC results, respectively, while Figure 5 gives a centerline comparison of gas density and velocities. The qualitative agreement in Figure 4 is good; however, there exist features of the results which warrant discussion. Near the centerline of the DK result, there exists a slight ‘bump’ in the density contour which does not exist in the DSMC result. This feature is found to be dependent on the number of radial, physical cells used at the orifice. In the current simulation, there are two cells in the radial direction: further refinement at this region would likely diminish this feature. Similar behavior has been identified in other simulations of a neutral flow near the centerline, and remains a difficulty with direct-kinetic methods.^{31,32}

Figure 5 shows excellent agreement in neutral density along the centerline; the axial velocity in the plume, however, exhibits a constant percent difference of approximately 2.8%. This owes to the fact that the ES-BGK operator is a simplified version of the full Boltzmann collision operator, which the DSMC code is able to approximate. The transitional nature of the flow at the orifice likely poses a challenge for the ES-BGK operator: this observation is consistent with other numerical studies, which report similar levels of error.³³ Figure 6 gives the Knudsen number along the centerline of the flow, using the cathode channel radius as the length scale. The plot demonstrates that, at the orifice, the flow is indeed transitional; the Knudsen number increases from $Kn \sim 0.01$ within the cathode channel to $Kn \sim 1$ just outside the orifice, thus illustrating the utility of a more general fluid description to accurately capture flow features. Special

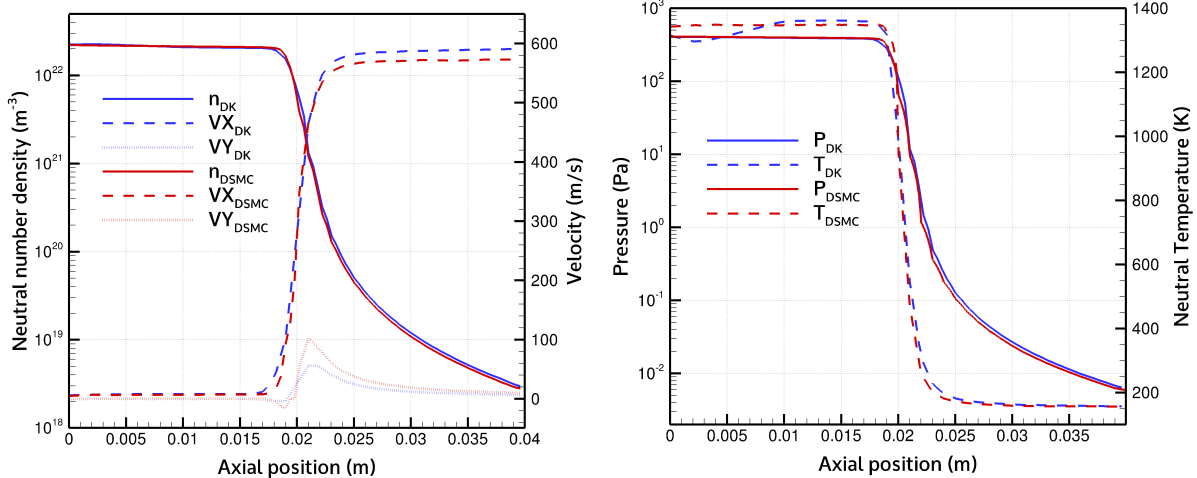


Figure 5: Centerline properties for neutral verification; density and velocities (left), pressure and temperature (right).

care is taken in determining suitable levels of refinement in velocity space, as results are very sensitive to this discretization. In the case of this axisymmetric expansion flow, the axial velocity is greatly overpredicted if there is not sufficient refinement in the velocity magnitude, ξ . The discretization in ξ is set based on previous simulations, which demonstrated a threshold refinement necessary to achieve mesh independence. In general, the results shown here indicate the neutral flow solver is verified with DSMC, and thus suitable for use in further cathode simulations. The ion routine is verified in a similar manner by considering a neutral flow and comparing with DSMC, though for brevity this comparison is not included here.

C. NSTAR Discharge Hollow Cathode

With the neutral solver verified using the NSTAR discharge cathode geometry, a full neutral-plasma simulation is completed. This case is run by first running only neutral particles until steady-state is reached. After this time, the ion and plasma routines are activated and run for another length of time. Specifically, this case uses identical conditions as given in Table 1 for the neutral pre-flow stage. The cathode is then run for another 25,000 time steps, with the ion and plasma parameters given in Table 2. The electron temperature is set to vary axially from 1eV to 4eV, based on experimental data from this cathode. An anode boundary is imposed at the upper plume, where the potential is set to $\phi = 20V$. The background plasma at simulation start is set to $n_i = 1 \times 10^{15} m^{-3}$ in order to facilitate ionization. No keeper is yet included in these simulations.

Figure 7 gives the plasma density and potential from four sources: i) the solver developed here, ii) the solver developed here with an assigned plume potential, iii) a multi-fluid code from [7], and iv) experimental data from [29]. It should be noted that the fluid electron model case used for comparison here does not include anomalous collisions to approximate IAT, which has been successful in describing bulk plasma parameters.³⁴ As is evident in Figure 7, the DK code is unable to find good agreement within the body of the cathode. There are many possible reasons

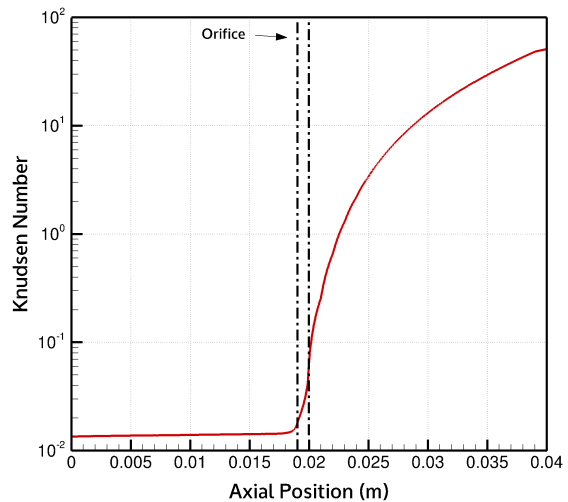


Figure 6: Neutral Knudsen number along the centerline. The orifice entrance and exit are given by the dashed lines.

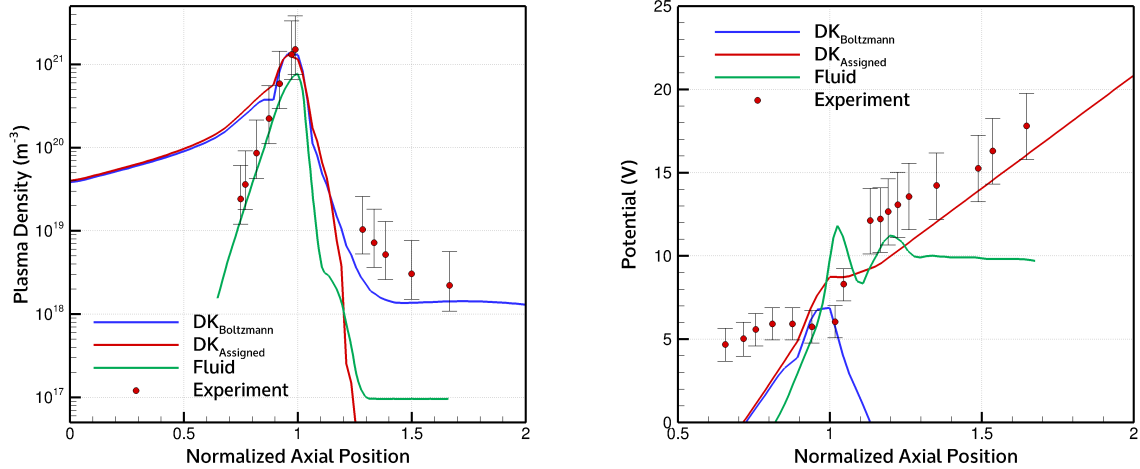


Figure 7: Comparison of centerline plasma properties. Results are plotted versus axial position normalized to orifice entrance.

for the large discrepancy here: for example, there is currently no sheath model implemented, such that ions will not have accelerated loss to the walls and thus remain present in a larger concentration. In addition, momentum exchange and charge exchange collisions are not taken into account here, which could have significant influence in this region as neutral and ion densities are relatively high. The code provides good agreement near the orifice region, where the plasma is believed to still be classically dominated, before expanding into the plume.

The plasma potential deviates significantly from both simulation results, especially in the plume. Indeed, the potential calculated from Equation 6 is dependent only on the ion density and electron temperature in these simulations, and therefore it is expected to drop significantly outside of the orifice. This potential drop results in a large axial electric field, which tends to accelerate the ions away from the cathode. In contrast, experimental evidence indicates a rise in potential as the anode is approached, which creates an electric field that opposes ion motion. At the same time, however, experimental evidence indicates there is a population of hot ions that accelerate, both radially and axially, as they evolve into the plume.¹³ Therefore, it is useful to look at ion velocities and temperatures in the plume region.

We see in Figure 8a that the ions are cool (~ 0.1 eV) within the cathode and remain cool for some time into the plume. After traveling around 10mm into the plume, the ions heat significantly to temperatures of ~ 5 eV. Additionally, we see that there is bulk ion backstreaming into the device wall, beginning around 7.5mm from the centerline. The ions in this region are comparatively hot, at a temperature of ~ 6 eV; while the keeper is not included in these simulations, this is the region where the keeper would reside. Thus, we observe a relatively energetic ion population which backstreams to the keeper, even without the inclusion of anomalous ion heating.

V_Z (m/s)	[-4000,6000]
V_R (m/s)	[-6000,6000]
V_θ (m/s)	[-2000,2000]
N_{V_Z}	40
N_{V_R}	48
N_{V_θ}	20
β	1.0
ϕ_o (V)	-20.0
n_o (m^{-3})	1×10^{16}

Table 2: Plasma Conditions

However, the unphysical electrostatic acceleration of the ions can skew the results and provide an overestimate of the ion energies. In order to provide a better comparison with experiment, a second case was run with an assigned potential profile in the plume. The potential is set to linearly increase from the orifice region to the simulation exit boundaries. The potential increases to 20V at the axial boundary, and by 20V towards the radial boundaries. Figure 8b gives the contour of this case, where we see significantly less heating of the ions in general. Rather than accelerating from the cathode orifice, the ions generally undergo recirculation in this region. There is also bulk back-streaming of the ions towards the cathode wall along

the entire surface. The bulk motion of the ions found in this case is likely a better representation of the ‘slow’ populations found in experimental sampling of ion motion. However, as seen in Figure 7, the assigned potential case severely underpredicts the plasma density in the plume region, and it is likely that a more detailed description of the plasma is necessary. Therefore, for further analyses here, the Boltzmann relation case results will be used to get a qualitative understanding of the plume ion kinetics.

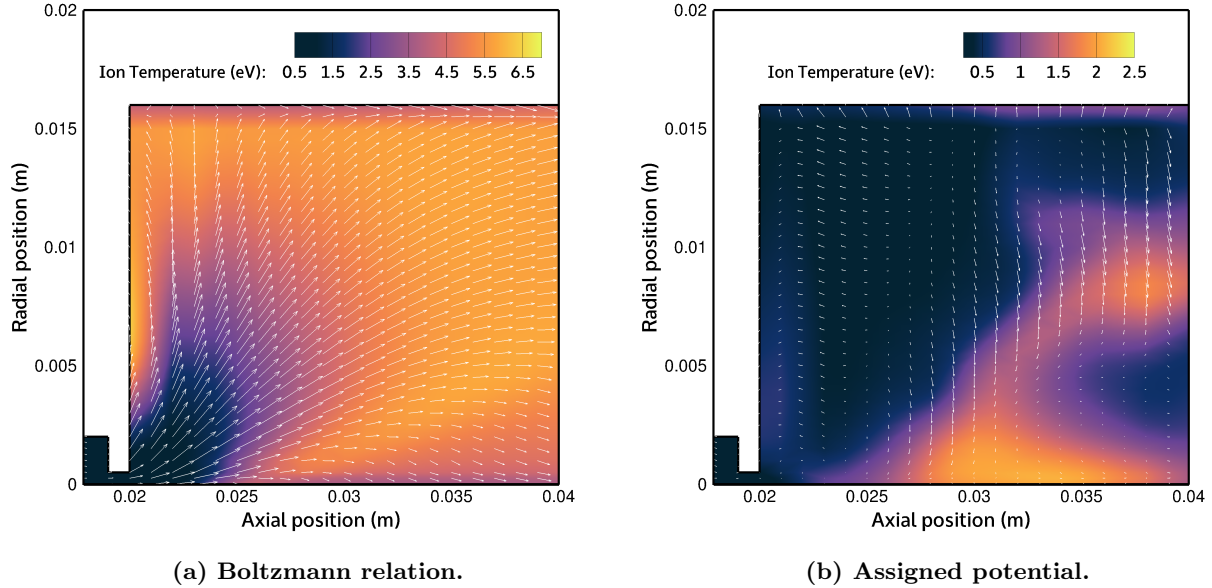


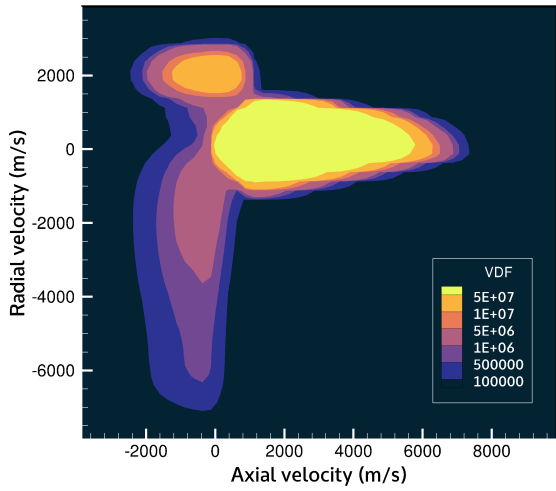
Figure 8: Plume ion temperature with overlaid ion velocity vectors.

To better understand how the ion population develops into the plume, the VDFs along the plume centerline are sampled. Figure 9 demonstrates the evolution of the axial-radial VDF at the $v_\theta = 0$ plane. The contour magnitudes are given in arbitrary units. In (a), we see a beam-like population of ions at the orifice exit plane, with a large axial bulk drift velocity. As the ions move into the plume, as in (b), the bulk axial drift has diminished significantly, and a large thermal spread of radial velocities is present. This thermal spread is likely due to the anode condition at the upper plume boundary generating high velocity downstreaming ions, and driving the radial temperature to be much higher than the axial temperature. In (c) and (d), as the ions continue downstream, the bulk drift in both the axial and radial directions increases. This can be attributed to both the potential gradient and the pressure gradient setup by the cathode. Thus, while the mechanisms which accelerate the ions are likely not consistent with those in experiment, the resulting heating and acceleration trends are similar.

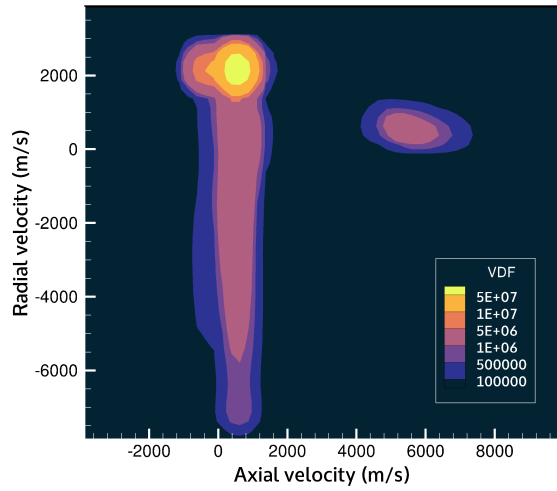
It is also useful to observe the ion energies which are present near the cathode keeper surface, as the ion energies are critically important in determining erosion rates. To do this, the ion VDFs are sampled along the cathode plume wall boundary and ion energy distribution functions (IEDFs) are generated. Figure 10 demonstrates that the ions exhibit large radial energies, but relatively small axial energies. As was the case for the large radial thermal spread on the centerline boundary, this is likely a result of the anode boundary condition placed at the upper plume. At all points along the wall considered, we see ions with radial energies up to $20eV$, which is the assigned anode boundary potential. There are no significant ion populations which exhibit axial energies in excess of $5eV$. Thus, we observe that the ions present near the keeper wall exhibit energies only up to the discharge potential. This indicates that there are other processes not captured in these simulations, such as IAT, which generate high energy ions capable of producing higher levels of erosion.

IV. Conclusions & Future Work

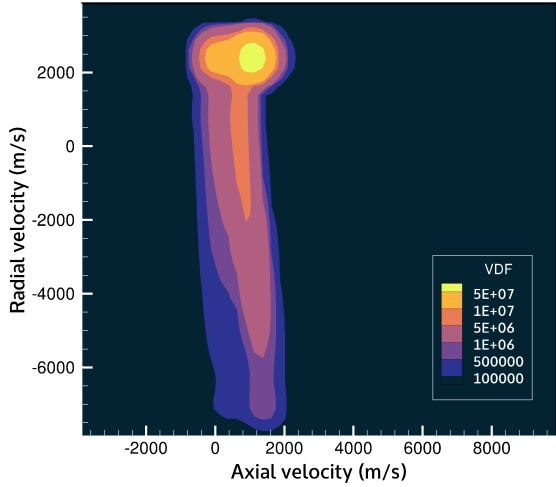
The development of an axisymmetric, deterministic kinetic solver was detailed here. The ES-BGK neutral collision algorithm was verified with a 1D Sod shock tube problem, while overall verification of the neutral flow solver was carried out by comparison with the DSMC code, MONACO. The schemes detailed were then applied to study the NSTAR discharge hollow cathode, utilizing a Boltzmann relation plasma. Results



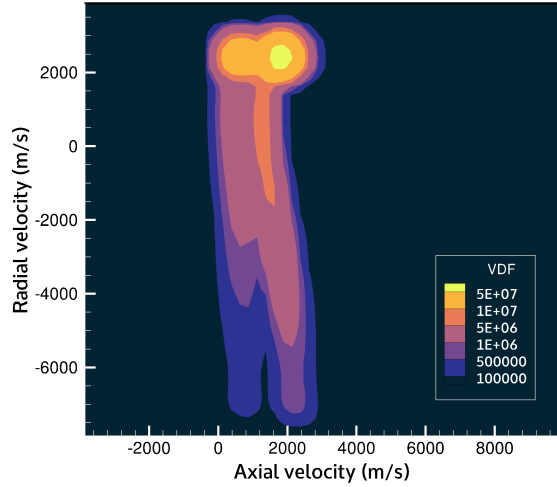
(a) $z = 2.0\text{cm}$



(b) $z = 2.5\text{cm}$

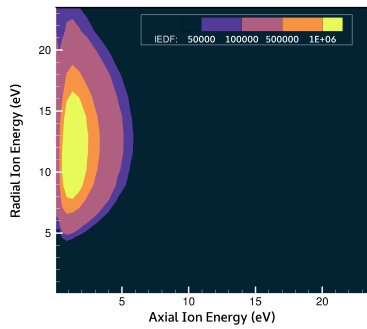


(c) $z = 3.0\text{cm}$

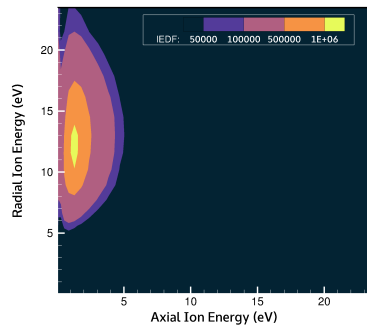


(d) $z = 3.5\text{cm}$

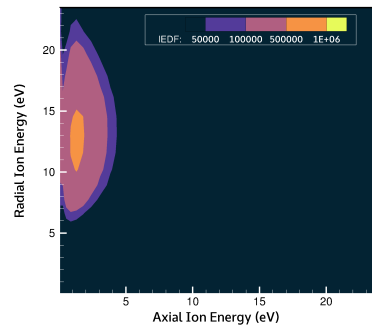
Figure 9: 2V ion VDFs along simulation centerline.



(a) $r = 0.65\text{cm}$



(b) $r = 0.75\text{cm}$



(c) $r = 0.85\text{cm}$

Figure 10: 2V IEDFs along simulation plume wall boundary.

demonstrate difficulty in obtaining agreement with the cathode plasma discharge measurements when using a Boltzmann relation plasma, so a more physical potential profile was assigned to observe ion dynamics in the plume. Simulated ion velocity vectors and ion temperatures in the cathode plume were compared for both cases. Ion VDFs were assessed along the plume centerline and found to both heat and accelerate, axially and radially. IEDFs were sampled along the cathode wall boundary, where no significant ion population with energies in excess of the discharge voltage were observed, thus indicating that some unresolved phenomenon, such as ion-acoustic turbulence, must be present in the physical system to generate such ions.

Accurate assessment of heavy particle dynamics in the plume region is especially important in understanding the processes which drive erosion of the cathode keeper. Ions with energies in excess of the discharge voltage have been identified in the plume, which are capable of eroding the cathode keeper and causing premature mission failure. The capability to capture the effect of ion-acoustic turbulence is necessary to better understand the plasma processes in the plume and their effect on the ion VDF, such as how a fast axially drifting ion population is generated. Future work with this simulation capability will be to include the effects of ion-acoustic turbulence to better resolve the plume plasma properties, requiring that electrons be modeled from first principles. Other relevant physics, such as atom-ion collisions, should also be included in the future.

V. Acknowledgments

The first author would like to thank Dr. Laurent Garrigues for insight and providing results for comparison, and Astrid Raisanen for useful discussions and collaboration. This work was supported through the National Defense Science and Engineering Graduate (NDSEG) Fellowship sponsored by the Air Force Office of Scientific Research (AFOSR).

References

- ¹John R. Brophy, Charles Garner, Barry Nakazono, Mike Marcucci, Mike Henry, and Don Noon. The Ion Propulsion System for Dawn. *39th AIAA/ASME/SAE/ASEE Joint Propulsion Conference and Exhibit*, (July):1–8, 2003.
- ²Ioannis G. Mikellides, Ira Katz, Richard R. Hofer, and Dan M. Goebel. Magnetic shielding of a laboratory Hall thruster. I. Theory and validation. *Journal of Applied Physics*, 115(4), 2014.
- ³Dan M. Goebel, Kristina K. Jameson, Ira Katz, and Ioannis G. Mikellides. Energetic Ion Production and Keeper Erosion in Hollow Cathode Discharges. *Proceedings of the International Electric Propulsion Conference 2005 (IEPC05)*, 2005.
- ⁴Maria Choi and Iain D. Boyd. Numerical Simulation of Keeper Erosion in a 6-kW Laboratory Hall Thruster. *34th International Electric Propulsion Conference*, pages 1–15, 2015.
- ⁵Amanda K. Ho, Benjamin A. Jorns, Ioannis G. Mikellides, Dan M. Goebel, and Alejandro Lopez Ortega. Wear Test Demonstration of a Technique to Mitigate Keeper Erosion in a High-Current LaB 6 Hollow Cathode. *52nd AIAA/SAE/ASEE Joint Propulsion Conference*, 2016.
- ⁶Ioannis G. Mikellides, Ira Katz, Dan M. Goebel, and James E. Polk. Hollow cathode theory and experiment. II. A two-dimensional theoretical model of the emitter region. *Journal of Applied Physics*, 98(11), 2005.
- ⁷Gaétan Sary, Laurent Garrigues, and Jean-Pierre Boeuf. Hollow cathode modeling: I. A coupled plasma thermal two-dimensional model. *Plasma Sources Science and Technology*, 26(5):55007, 2017.
- ⁸Kenichi Kubota, Y. Oshio, H. Watanabe, Shinatora Cho, Y. Ohkawa, and Ikkoh Funaki. Hybrid - PIC Simulation on Plasma Flow of Hollow Cathode. *Proceedings of the 34th International Electric Propulsion Conference*, pages IEPC–2015–15, 2015.
- ⁹Pierre-Yves C. R. Taunay, Christopher J. Wordingham, and Edgar Choueiri. An empirical scaling relationship for the total pressure in hollow cathodes. *2018 Joint Propulsion Conference*, (July):1–12, 2018.
- ¹⁰Benjamin A. Jorns, Dan M. Goebel, and Ioannis G. Mikellides. Investigation of Energetic Ions in a 100-A Hollow Cathode. *50th AIAA/ASME/SAE/ASEE Joint Propulsion Conference*, pages 1–17, 2014.
- ¹¹Christopher A. Dodson, Daniel Perez-Grande, Benjamin A. Jorns, Dan M. Goebel, and Richard E. Wirz. Laser-induced fluorescence measurements of energetic ions in a 100-A LaB6 hollow cathode plume. *52nd AIAA/SAE/ASEE Joint Propulsion Conference, 2016*, pages 1–15, 2016.
- ¹²Christopher A. Dodson, Daniel Perez-Grande, Benjamin A. Jorns, Dan M. Goebel, and Richard E. Wirz. Ion Heating Measurements on the Centerline of a High-Current Hollow Cathode Plume. *Journal of Propulsion and Power*, 34(5), 2018.
- ¹³Christopher A. Dodson, Benjamin A. Jorns, and Richard E. Wirz. Measurements of ion velocity and wave propagation in a hollow cathode plume. *Plasma Sources Science and Technology*, 28(6):065009, jun 2019.
- ¹⁴Marcel P. Georgin, Benjamin A. Jorns, and Alec D. Gallimore. An Experimental and Theoretical Study of Hollow Cathode Plume Mode Oscillations. *35th International Electric Propulsion Conference*, pages 1–8, 2017.
- ¹⁵Ioannis G. Mikellides, Pablo Guerrero, Alejandro Lopez Ortega, and James E. Polk. Spot-to-plume Mode Transition Investigations in the HERMeS Hollow Cathode Discharge Using Coupled 2-D Axisymmetric Plasma-Thermal Simulations. *2018 Joint Propulsion Conference*, pages 1–23, 2018.

- ¹⁶Marcel P. Georjin, Benjamin A. Jorns, and Alec D. Gallimore. Time-varying non-classical electron resistivity in a hollow cathode plume. *2019 AIAA Propulsion and Energy Forum*, (August):1–13, 2019.
- ¹⁷Iain D. Boyd and Thomas E. Schwartzentruber. *Nonequilibrium gas dynamics and molecular simulation*. Cambridge University Press, Cambridge, 2017.
- ¹⁸C K Birdsall and A B Langdon. *Plasma physics via computer simulation*. IOP Publishing, 1991.
- ¹⁹Kentaro Hara, Iain D. Boyd, and Vladimir I. Kolobov. One-dimensional hybrid-direct kinetic simulation of the discharge plasma in a Hall thruster. *Physics of Plasmas*, 19(11), 2012.
- ²⁰Astrid Raisanen, Kentaro Hara, and Iain D. Boyd. Comparing Two-Dimensional, Axisymmetric, Hybrid-Direct Kinetic and Hybrid-Particle-in-Cell Simulations of the Discharge Plasma in a Hall Thruster. *52nd AIAA/SAE/ASEE Joint Propulsion Conference*, pages 1–14, 2016.
- ²¹G. V. Vogman, Uri Shumlak, and P. Colella. Conservative fourth-order finite-volume Vlasov-Poisson solver for axisymmetric plasmas in cylindrical $(r, vr, v\theta)$ phase space coordinates. *Journal of Computational Physics*, 373:877–899, 2018.
- ²²Kentaro Hara. *Development of Grid-Based Direct Kinetic Method and Hybrid Kinetic-Continuum Modeling of Hall Thruster Discharge Plasmas*. Dissertation, University of Michigan, 2015.
- ²³Dan M. Goebel and Ira Katz. Fundamentals of Electric Propulsion: Ion and Hall Thrusters. *Fundamentals of Electric Propulsion: Ion and Hall Thrusters*, pages 1–507, 2008.
- ²⁴Luc Mieussens. Discrete-Velocity Models and Numerical Schemes for the Boltzmann-BGK Equation in Plane and Axisymmetric Geometries. *Journal of Computational Physics*, 162(2):429–466, 2000.
- ²⁵Sandra Pieraccini and Gabriella Puppo. Implicit-explicit schemes for BGK kinetic equations. *Journal of Scientific Computing*, 32(1):1–28, 2007.
- ²⁶Gary A. Sod. A survey of several finite difference methods for systems of nonlinear hyperbolic conservation laws. *Journal of Computational Physics*, 31:1–31, 1978.
- ²⁷Stefan Dietrich and Iain D. Boyd. Scalar and parallel optimized implementation of the direct simulation Monte Carlo method. *Journal of Computational Physics*, 126(2):328–342, 1996.
- ²⁸John R. Brophy. NASA’s deep space 1 ion engine (plenary). *Review of Scientific Instruments*, 73(2 II):1071, 2002.
- ²⁹Dan M. Goebel, Kristina K. Jameson, Ira Katz, and Ioannis G. Mikellides. Plasma potential behavior and plume mode transitions in hollow cathode discharges. *30th International Electric Propulsion Conference*, pages 1–9, 2007.
- ³⁰Ioannis G. Mikellides, Ira Katz, Dan M. Goebel, James E. Polk, and Kristina K. Jameson. Plasma processes inside dispenser hollow cathodes. *Physics of Plasmas*, 13(6), 2006.
- ³¹Kentaro Hara and Kyle M. Hanquist. Test cases for grid-based direct kinetic modeling of plasma flows. *Plasma Sources Science and Technology*, 27(6), 2018.
- ³²Astrid L. Raisanen and Iain D. Boyd. Boundary conditions for a two-dimensional direct kinetic simulation of a Hall thruster. *36th International Electric Propulsion Conference*, 613, 2019.
- ³³Jianping Meng, Yonghao Zhang, Nicolas G. Hadjiconstantinou, Gregg A. Radtke, and Xiaowen Shan. Lattice ellipsoidal statistical BGK model for thermal non-equilibrium flows. *Journal of Fluid Mechanics*, 718:347–370, 2013.
- ³⁴Gaétan Sary, Laurent Garrigues, and Jean-Pierre Boeuf. Hollow cathode modeling: II. Physical analysis and parametric study. *Plasma Sources Science and Technology*, 26(5):55008, 2017.